J. Fluid Mech. (2013), *vol.* 733, *pp.* 414–438.
doi:10.1017/jfm.2013.399

Topological evolution in compressible turbulent boundary layers

You-Biao Chu and Xi-Yun Lu†

Department of Modern Mechanics, University of Science and Technology of China, Hefei, Anhui 230026, China

(Received 1 February 2013; revised 26 July 2013; accepted 29 July 2013)

Topological evolution of compressible turbulent boundary layers at Mach 2 is investigated by means of statistical analysis of the invariants of the velocity gradient tensor based on the direct numerical simulation database. The probability density functions of the rate of change of the invariants exhibit the -3 power-law distribution in the region of large Lagrangian derivative of the invariants in the inner and outer layers. The topological evolution is studied by conditional mean trajectories for the evolution of the invariants. The trajectories illustrate inward-spiralling orbits around and converging to the origin of the space of invariants in the outer layer, while they are repelled by the vicinity of the origin and converge towards a limit cycle in the inner layer. The compressibility effect on the mean topological evolution is studied in terms of the 'incompressible', compressed and expanding regions. It is found that the mean evolution of flow topologies is altered by the compressibility. The evolution equations of the invariants are derived and the relevant dynamics of the mean topological evolution are analysed. The compressibility effect is mainly related to the pressure effect. The mutual-interaction terms among the invariants are the root of the clockwise spiral behaviour of the local flow topology in the space of invariants.

Key words: compressible boundary layers, turbulent boundary layers

1. Introduction

The velocity gradient tensor (VGT) describes a variety of geometrical and statistical phenomena of small-scale motions of turbulence, such as the alignment of vorticity with respect to the strain-rate eigenvectors, rates of deformation and the shape of fluid material volumes, energy cascades and intermittency (Meneveau 2011). The study of velocity gradient dynamics is crucial to the understanding of the kinematics and dynamics of turbulent motions (Frisch 1995; Sagaut & Cambon 2008; Tsinober 2009). Moreover, the dynamics can be used to model the subgrid-scale stress tensor (Cantwell 1992; Chertkov, Pumir & Shraiman 1999; van der Bos *et al.* 2002; Wang *et al.* 2006; Li *et al.* 2009).

Based on the topological approach proposed by Chong, Perry & Cantwell (1990), the invariants of VGT can be employed to classify the local topology of any point in the flow in terms of critical point theory (Perry & Chong 1987). This topological methodology was first applied to the study of compressible and incompressible

† Email address for correspondence: xlu@ustc.edu.cn

turbulent mixing layers (Chen *et al.* 1990). Then, the investigations of the statistical properties in the invariants space have been performed mainly based on numerical simulations (e.g. Soria *et al.* 1994; Blackburn, Mansour & Cantwell 1996; Chong *et al.* 1998; Wang & Lu 2012). Moreover, few experiments have been performed to deal with the behaviours of the invariants of the VGT in incompressible turbulent boundary layers (Andreopoulos & Honkan 2001; Elsinga & Marusic 2010). We should indicate that the reason for the lack of experimental studies is because of the difficulty associated with measuring the VGT with sufficient precision and spatial resolution. Recently, the accuracy of tomographic particle image velocimetry for measurements of the turbulent boundary layer has been investigated by Atkinson *et al.* (2011). As the smallest resolvable structures estimated by the experiment are larger than the smallest expected coherent structures, the spatial derivatives of the velocity field measured in the turbulent boundary layer cannot be accurately obtained for the temporal evolution of these quantities as considered in this study. Thus, the most accurate method, such as direct numerical simulation (DNS), is the most reliable avenue to study the evolution of the topology of the turbulent boundary layer.

The dynamical behaviour of the VGT is of fundamental importance in turbulent flow. Thus, the Lagrangian evolution of the invariants of the VGT has been studied using conditional mean trajectories (CMTs). Martín *et al.* (1998) and Ooi *et al.* (1999) investigated the evolution of flow topology of incompressible homogeneous isotropic turbulence using the CMTs in the plane of the second (Q) and third (R) invariants (i.e. the Q–R plane), in which the fluid particles were observed to exhibit a clockwise spiral with a stable focus at the origin. Chacin & Cantwell (2000) examined the Lagrangian behaviour of the invariants for a low-Reynolds-number turbulent boundary layer by keeping track of the evolution of these scalars in the Q–R plane. For most regions of the boundary layer, the fluid particles were observed to move towards the origin following asymptotes without the spiralling pattern, which was observed in homogeneous isotropic turbulence. The only exception to this behaviour was in the viscous sublayer, but the spiralling did not show asymptotic behaviour. The CMTs for higher-Reynolds-number incompressible turbulent boundary layers have been investigated (Bermejo-Moreno *et al.* 2010; Elsinga & Marusic 2010; Mizuno, Atkinson & Soria 2011; Atkinson *et al.* 2012). The trajectories in the outer region reveal inward-spiralling orbits around the origin and converging to the origin (Elsinga & Marusic 2010). In the buffer layer, the trajectories are repelled by the vicinity of the origin, and converge towards a limit cycle (Mizuno *et al.* 2011). The mean Lagrangian evolution of a turbulent boundary layer at momentum-thickness Reynolds number $Re_\theta = 730$–1954 has been investigated by Atkinson *et al.* (2012) using data from a DNS performed by Wu & Moin (2010). They found that the CMTs for strong gradients in the regions of the boundary layer pass around a focus at the origin and asymptote towards the right-hand side of a saddle point located near the right-hand side of the line dividing unstable focal and unstable nodal structures. Closer to the origin with weaker gradients, the CMTs follow an almost periodic clockwise spiralling evolution. In addition, Lüthi, Holzner & Tsinober (2009) expanded the Q–R plane to three dimensions by the decomposition of R into its strain production and enstrophy production terms and observed that the non-locality plays an important role in the evolution of the velocity gradients.

As the structures of the invariants are associated with geometrical features of small-scale motions, the modelling equations for representing the evolution of the invariants have been developed in an attempt to simulate and study the characteristics of coherent structures in turbulence. Restricted Euler (RE) dynamics has been obtained

by neglecting viscous diffusion and the anisotropic effect of pressure, but involves unphysical finite-time singularities (Vieillefosse 1982; Cantwell 1992). In order to regularize the RE dynamics, a stochastic diffusion model with prescribed log-normal dissipation was discussed by Girimaji & Pope (1990). Also a linear damping model for the viscous term was proposed by Martin *et al.* (1997). The recent fluid deformation approximation has been proposed by Chevillard & Meneveau (2006) and can be considered as a simplified version of the tetrad model (Chertkov *et al.* 1999) with elements of the Lagrangian linear diffusion model (Jeong & Girimaji 2003).

Compared with the research into flow topology in incompressible turbulent flows described above, the relevant study of compressible turbulence is limited. Chen *et al.* (1990) investigated the flow topology in the Q_S–Q_W plane for compressible mixing layers. Then, Pirozzoli & Grasso (2004) studied the effect of the initial compressibility of compressible isotropic turbulence on the flow topology in the plane of the second (Q^*) and third (R^*) invariants of the anisotropic part of the VGT. Lee, Girimaji & Kerimo (2009) indicated that the effects of the pressure Hessian in the equation of the VGT require different modelling approaches for compressible turbulence. Suman & Girimaji (2009, 2010) developed a homogenized Euler equation for describing turbulent velocity gradient dynamics of an isentropic compressible calorically perfect gas. Then they also analysed the influence of Mach number and dilatation rate on the velocity gradient dynamics in decaying compressible isotropic turbulence (Suman & Girimaji 2012). Recently, the invariants of the VGT are investigated statistically for compressible turbulent boundary layer at Mach 2 (Wang & Lu 2012). The compressibility effect on the statistical properties of the topologies has been analysed in terms of the 'incompressible', compressed and expanding regions. To the best of the authors' knowledge, however, the relevant study of the topological evolution in compressible turbulent boundary layer has never been performed.

In this paper, the statistical properties of the compressible turbulent boundary layer are investigated based on the DNS database (Wang & Lu 2012). The local flow topological evolution and the relevant Lagrangian models are analysed in terms of the invariants of the VGT. The purpose of this study is to achieve an improved understanding of some of the fundamental topological evolution behaviours in compressible turbulent boundary layers.

This paper is organized as follows. The DNS database is briefly described in § 2. Lagrangian equations for the invariants of the VGT are derived in § 3. Detailed results are discussed in § 4 and concluding remarks are finally addressed in § 5.

2. DNS database

To study topological evolution in a compressible turbulent boundary layer, we have used the DNS database obtained in our previous work (Wang & Lu 2012) for the present study. The relevant parameters are briefly described as follows. Here, we investigate a supersonic turbulent boundary layer with the free-stream Mach number $Ma = 2$ and Reynolds number $Re_{\delta_0} = 13\,500$ based on the free-stream parameters and the boundary-layer thickness at the inlet (δ_0). A fully developed turbulence is considered with the momentum-thickness Reynolds number region of $Re_\theta = 1280$–1550. The corresponding friction Reynolds number Re_τ varies from 300 to 360.

The equations are numerically solved by a seventh-order weighted essentially non-oscillatory scheme for the convective terms (Jiang & Shu 1996) and a sixth-order central difference scheme for the viscous terms. The temporal integration is performed

using a fourth-order Runge–Kutta algorithm (Shu & Osher 1988). The relevant numerical strategy has been verified to be reliable in the simulation of compressible turbulent boundary layers (e.g. Pirozzoli, Grasso & Gatski 2004; Pirozzoli, Bernardini & Grasso 2008). Detailed descriptions of the initial and boundary conditions have been given in our previous paper (Wang & Lu 2012). Essentially, we have carefully examined the physical model and numerical approach and have verified that the calculated results are reliable by comparing the calculated results with previous data in terms of the mean velocity, Reynolds stress and root-mean-square (r.m.s.) vorticity components (Wang & Lu 2012).

Based on the mean velocity profile along the wall-normal direction y (Wang & Lu 2012), the boundary layer is then classified into four regions by means of the standard terminology (Pope 2000): viscous sublayer ($0 < y^+ < 7$), buffer layer ($7 < y^+ < 40$), logarithmic layer ($40 < y^+ < 140$) and defect layer ($y^+ > 140$), where the superscript '+' denotes the quantities in wall units defined in terms of the friction velocity $u_\tau = (\tau_w/\rho_w)^{1/2}$ and the viscous length scale $\delta_\upsilon = \nu_w/u_\tau$ evaluated at the wall. Moreover, the viscous sublayer and buffer layer are usually referred to as the 'inner layer' and the logarithmic layer and defect layer as the 'outer layer' (Pirozzoli *et al.* 2008). The statistical quantities are obtained in terms of 1000 flow field samples over $\sim 5\delta_0/u_\tau$ separated by $0.1\delta_0/U_\infty$ after the flow reaches a statistically steady state, where U_∞ is the free-stream speed.

In addition, to examine the influence of Mach number, a complemental case for compressible turbulent boundary layer at Mach 4.9, which was numerically investigated by Duan, Beekman & Martín (2011), is also considered in this study. The DNS database of compressible turbulent boundary layers at $Ma = 4.9$ with the momentum thickness Reynolds number $Re_\theta = 6600$–6800 and frictional Reynolds number $Re_\tau = 380$–415 was obtained and analysed in our recent work (Chu 2013). We have essentially identified that the statistical properties of local flow topological evolution are qualitatively similar for both of the Mach numbers. Unless otherwise stated, the results presented in the paper correspond to $Ma = 2$.

To clearly present the post-process, some symbols used in this paper are introduced as follows. The Reynolds average of a variable f in time and in space along the streamwise (x) and spanwise (z) directions is denoted by $\bar{f}$, and the corresponding fluctuation is defined as $f' = f - \bar{f}$. The subscript '*rms*' denotes the r.m.s. value of the relevant quantity.

3. Lagrangian equations of the invariants

3.1. *Definitions of the invariants*

The eigenvalues Λ_i of the VGT $\boldsymbol{A}$ with components $A_{ij} = \partial u_i/\partial x_j$ are obtained as solutions of the characteristic equation

$$\Lambda_i^3 + P\Lambda_i^2 + Q\Lambda_i + R = 0, \tag{3.1}$$

where P, Q and R are the first, second and third invariants of $\boldsymbol{A}$, defined by

$$P = -\mathrm{tr}(\boldsymbol{A}) = -S_{ii} = -\vartheta, \tag{3.2a}$$

$$Q = \tfrac{1}{2}([\mathrm{tr}(\boldsymbol{A})]^2 - \mathrm{tr}(\boldsymbol{A}^2)) = \tfrac{1}{2}(P^2 - S_{ij}S_{ji} - W_{ij}W_{ji}), \tag{3.2b}$$

$$R = -\det(\boldsymbol{A}) = \tfrac{1}{3}(-P^3 + 3PQ - S_{ij}S_{jk}S_{ki} - 3W_{ij}W_{jk}S_{ki}), \tag{3.2c}$$

Sector	Acronym	Description
S1	UFC	Unstable focus compressing
S2	UN/S/S	Unstable node/saddle/saddle
S3	SN/S/S	Stable node/saddle/saddle
S4	SFS	Stable focus stretching
S5	SFC	Stable focus compressing
S6	SN/SN/SN	Stable node/stable node/stable node
S7	UFS	Unstable focus stretching
S8	UN/UN/UN	Unstable node/unstable node/unstable node

TABLE 1. Summary of the acronyms of various flow topologies in the P–Q–R space.

where ϑ represents the dilatation, $S_{ij} = (A_{ij} + A_{ji})/2$ is the symmetric strain-rate tensor $\boldsymbol{S}$ and $W_{ij} = (A_{ij} - A_{ji})/2$ is the skew-symmetric rotation-rate tensor $\boldsymbol{W}$. The invariants of $\boldsymbol{S}$ and $\boldsymbol{W}$ are then given by

$$P_S = P = -S_{ii}, \quad Q_S = \tfrac{1}{2}(P_S^2 - S_{ij}S_{ji}), \quad R_S = \tfrac{1}{3}(-P_S^3 + 3P_SQ_S - S_{ij}S_{jk}S_{ki}), \tag{3.3}$$

$$P_W = 0, \quad Q_W = -\tfrac{1}{2}W_{ij}W_{ji}, \quad R_W = 0. \tag{3.4}$$

Thus, we can obtain

$$Q = Q_S + Q_W, \quad R = R_S - \tfrac{1}{4}\omega_i S_{ij}\omega_j, \tag{3.5}$$

where ω_i is vorticity. Note that Q_W is positive definite and Q_S is negative definite. The discriminant of $\boldsymbol{A}$ is given by

$$\Delta = \tfrac{27}{4}R^2 + \left(P^3 - \tfrac{9}{2}PQ\right)R + \left(Q^3 - \tfrac{1}{4}P^2Q^2\right). \tag{3.6}$$

Further, the flow topology of turbulent flow can be investigated in P–Q–R space using critical point terminology (Perry & Chong 1987; Chong *et al.* 1990). The surface $\Delta = 0$ divides the space into two regions. In the region $\Delta > 0$, $\boldsymbol{A}$ has one real and two complex-conjugate eigenvalues; in the region $\Delta < 0$, $\boldsymbol{A}$ has three real, distinct eigenvalues. The surface $\Delta = 0$ can be split into two surfaces r_{1a} and r_{1b}, which osculate to form a cusp and are expressed by

$$\tfrac{1}{3}P(Q - \tfrac{2}{9}P^2) - \tfrac{2}{27}(-3Q + P^2)^{3/2} - R = 0, \tag{3.7a}$$

$$\tfrac{1}{3}P(Q - \tfrac{2}{9}P^2) + \tfrac{2}{27}(-3Q + P^2)^{3/2} - R = 0. \tag{3.7b}$$

In the region $\Delta > 0$, $\boldsymbol{A}$ has purely imaginary eigenvalues on the surface r_2, which is described by

$$PQ - R = 0. \tag{3.8}$$

Moreover, the flow pattern is two-dimensional on the surface $R = 0$ (Chong *et al.* 1990). Thus, the surfaces r_{1a}, r_{1b}, r_2 and $R = 0$ divide the P–Q–R space into different regions, and each of these regions corresponds to a topology. It is convenient to analyse the flow topology in the Q–R plane for a selected value of P (Suman & Girimaji 2010; Wang & Lu 2012). For $P = 0$, four topologies are identified as schematically exhibited in figure 1(*a*). For $P > 0$ and $P < 0$, the Q–R plane is divided into six regions and the corresponding topologies are shown in figure 1(*b,c*), respectively. Furthermore, the description of the topologies and the corresponding acronym are given in table 1.

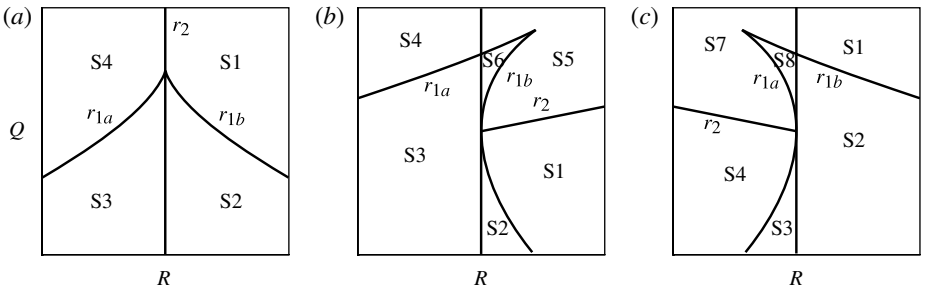

FIGURE 1. The topological classification in the Q–R plane for (*a*) $P = 0$, (*b*) $P > 0$ and (*c*) $P < 0$. The topologies and corresponding acronyms are listed in table 1.

3.2. *Evolution equations of the invariants*

The time evolution of $\boldsymbol{A}$ following fluid particles can be obtained by taking the gradient of the Navier–Stokes equations (e.g. Cantwell 1992; Martín *et al.* 1998; Ooi *et al.* 1999; Meneveau 2011). The resulting equation reads

$$\frac{\mathrm{D}A_{ij}}{\mathrm{D}t} + A_{ik}A_{kj} = -H_{ij} - B_{ij} + V_{ij}, \tag{3.9}$$

where $\mathrm{D}/\mathrm{D}t$ denotes the Lagrangian material derivative, B_{ij}, V_{ij} and H_{ij} represent the baroclinic tensor, viscous tensor and pressure Hessian tensor, respectively, and are defined by

$$H_{ij} = \frac{1}{\rho}\frac{\partial^2 p}{\partial x_i \partial x_j}, \quad B_{ij} = \frac{1}{\rho^2}\frac{\partial p}{\partial x_i}\frac{\partial \rho}{\partial x_j}, \quad V_{ij} = \frac{\partial}{\partial x_j}\left[\frac{1}{\rho}\left(\frac{\partial \boldsymbol{\sigma}_{ik}}{\partial x_k}\right)\right], \tag{3.10}$$

and $\boldsymbol{\sigma}_{ik}$ is the viscous stress tensor.

Based on the definitions of P, Q and R as well as (3.9), the evolution equations for P, Q and R are derived as

$$\frac{\mathrm{D}P}{\mathrm{D}t} = (P^2 - 2Q) + \mathrm{tr}(\boldsymbol{H}) + \mathrm{tr}(\boldsymbol{B}) - \mathrm{tr}(\boldsymbol{V}) = PS + PH + PB + PV, \tag{3.11}$$

$$\begin{aligned}\frac{\mathrm{D}Q}{\mathrm{D}t} &= (PQ - 3R) + (P\,\mathrm{tr}(\boldsymbol{H}) + \boldsymbol{S} : \boldsymbol{H}) + (P\,\mathrm{tr}(\boldsymbol{B}) + (\boldsymbol{S} - \boldsymbol{W}) : \boldsymbol{B}) \\ &\quad - (P\,\mathrm{tr}(\boldsymbol{V}) + (\boldsymbol{S} - \boldsymbol{W}) : \boldsymbol{V}) = QS + QH + QB + QV,\end{aligned} \tag{3.12}$$

and

$$\begin{aligned}\frac{\mathrm{D}R}{\mathrm{D}t} &= PR + \left(P(\boldsymbol{S} : \boldsymbol{H}) + Q\,\mathrm{tr}(\boldsymbol{H}) + (\boldsymbol{S}^2 + \boldsymbol{W}^2) : \boldsymbol{H}\right) + (P(\boldsymbol{S} - \boldsymbol{W}) : \boldsymbol{B} + Q\,\mathrm{tr}(\boldsymbol{B}) \\ &\quad + (\boldsymbol{S} - \boldsymbol{W})^2 : \boldsymbol{B}) - (P(\boldsymbol{S} - \boldsymbol{W}) : \boldsymbol{V} + Q\,\mathrm{tr}(\boldsymbol{V}) + (\boldsymbol{S} - \boldsymbol{W})^2 : \boldsymbol{V}) \\ &= RS + RH + RB + RV.\end{aligned} \tag{3.13}$$

The meanings of the terms in (3.11)–(3.13) are described as follows: PS, QS and RS are the mutual-interaction terms among the invariants; PH, QH and RH are the contributions due to the pressure Hessian; PB, QB and RB account for the baroclinic effect; PV, QV and RV are the viscous effect. Note that the non-local part of the pressure, i.e. the trace of the pressure Hessian, is expressed by not only the local velocity gradients as given for incompressible flow, but also the time rate of change of dilatation in (3.11). The pressure Hessian is therefore considered as a whole.

The transport equation for the enstrophy ($Q_W = \omega_i\omega_i/4$) is given by

$$\frac{\mathrm{D}Q_W}{\mathrm{D}t} = 2(\boldsymbol{S}:\boldsymbol{W}^2) - (\boldsymbol{W}:\boldsymbol{B}) + \boldsymbol{W}:\boldsymbol{V} = WS + WB + WV. \tag{3.14}$$

The rate of dissipation of mechanical energy per unit mass of fluid (Batchelor 1967) can be represented as

$$\Phi = 2\nu\left(S_{ij}S_{ij} - \tfrac{1}{3}P^2\right) = -4\nu\left(Q_S - \tfrac{1}{3}P^2\right). \tag{3.15}$$

Therefore, the dissipation rate of mechanical energy is proportional to $Q_S - P^2/3$, under the assumption of weak variation of the viscosity coefficient. The transport equation of Q_S is given by

$$\begin{aligned}\frac{\mathrm{D}Q_S}{\mathrm{D}t} &= \left(P(P^2 - 2Q) + \boldsymbol{S}:\boldsymbol{S}^2 + \boldsymbol{S}:\boldsymbol{W}^2\right) + (P\,\mathrm{tr}(\boldsymbol{H}) + \boldsymbol{S}:\boldsymbol{H}) \\ &\quad + (P\,\mathrm{tr}(\boldsymbol{B}) + \boldsymbol{S}:\boldsymbol{B}) - (P\,\mathrm{tr}(\boldsymbol{V}) + \boldsymbol{S}:\boldsymbol{V}) \\ &= SS + SH + SB + SV. \end{aligned} \tag{3.16}$$

The corresponding terms in (3.14) and (3.16) have the following meanings (Pirozzoli & Grasso 2004): WS is the vortex stretching; SS is the term related to the velocity gradient in which $P(P^2 - 2Q)$ is the direct effect of compressibility and $\boldsymbol{S}:\boldsymbol{S}^2$ is the self-amplification of the strain-rate tensor; SH is the action of the pressure Hessian tensor which is the same as the term QH in (3.12); WB and SB are the baroclinic effects; WV and SV account for the viscous actions.

The dynamics of the invariants can be also investigated in a Lagrangian frame of reference moving with a fluid particle by means of their material derivatives (Elsinga & Marusic 2010),

$$\frac{\mathrm{D}Iv}{\mathrm{D}t} = \frac{\partial Iv}{\partial t} + u\frac{\partial Iv}{\partial x} + v\frac{\partial Iv}{\partial y} + w\frac{\partial Iv}{\partial z}, \tag{3.17}$$

where Iv represents the invariants P, Q and R, respectively. Note that all of the terms on the right-hand side depend only on the velocity field. Therefore, (3.17) can be evaluated directly for the data and used to validate the calculations of the evolution (3.11)–(3.13). In the present study, the temporal derivative in (3.17) is approximated by a fourth-order central difference scheme, and all spatial derivatives are discretized by a sixth-order central difference scheme.

4. Results and discussion

The statistical properties of the mean velocity gradient and fluctuating velocity gradient are first investigated. Figure 2 shows the mean value of velocity gradient and the r.m.s. value of fluctuating velocity gradient. It is seen that the r.m.s. value of fluctuating velocity gradient is significantly larger than the mean value of velocity gradient within the boundary layer, except for $\partial u/\partial y$. As shown in figure 2(*b*), the value of $\overline{\partial u/\partial y}$ is larger than that of $(\partial u/\partial y)'_{rms}$ in the viscous sublayer, decays rapidly in the buffer layer and becomes smaller than $(\partial u/\partial y)'_{rms}$ in the outer layer. These characters indicate that the fluctuation in velocity gradient is significant relative to the mean flow in the outside region of the viscous sublayer. Similar to the previous investigations (e.g. Elsinga & Marusic 2010; Atkinson *et al.* 2012), the total velocity gradient including the mean and fluctuating velocity gradient can only describe the local flow topology of fluid particles in compressible turbulent boundary layers. Thus,

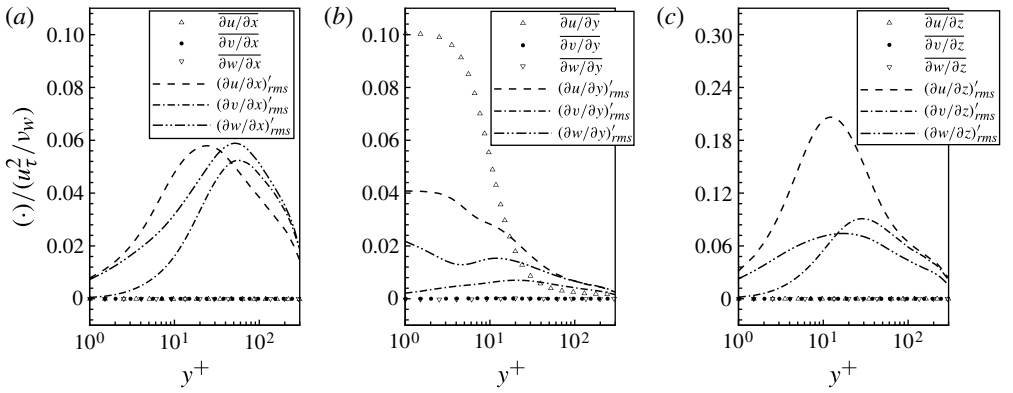

FIGURE 2. Distributions of the mean velocity gradient and the r.m.s. value of the fluctuating velocity gradient along the wall-normal direction. Here, u, v and w represent the streamwise, wall-normal and spanwise velocity components, respectively.

the flow topological evolution in the following analysis is based on the invariants of total velocity gradient.

4.1. *Probability density functions of the rate of change of invariants*

To investigate the statistical properties of local topological evolution, the p.d.f.s of the rate of change of the invariants are shown in figure 3. Here the Lagrangian material derivatives are normalized by the quantities related to $\langle Q_W \rangle$, where $\langle\ \ \rangle$ means the average in time and in space along the streamwise and spanwise directions, and the time t is normalized by $\langle Q_W \rangle^{-1/2}$. Moreover, Suman & Girimaji (2009) have employed local quantities related to A^2 $(=A_{ij}A_{ij})$ to normalize the invariants and the time. As we need to study the transformation from the invariants space into the physical space below, the average quantities related to $\langle Q_W \rangle$ are thus used in this study, following Martín *et al.* (1998). It is seen from figure 3 that the profiles exhibit nearly symmetric behaviour in the inner and outer layers, consistent with the previous findings (Elsinga & Marusic 2010). Moreover, after calculating the skewness factor for the invariants at different wall-normal locations, it is identified that the skewness factors are always less than 0.1, indicating that the skewness is very weak (e.g. Kim, Moin & Moser 1987). The occurrence possibilities of the increase of the invariants are in balance with those of the decrease of the invariants to maintain the equilibrium state. Furthermore, as the high-order spatial derivatives appear in the evolution equations (3.11)–(3.13), the relevant simulations are thus examined by comparison with the results obtained directly by the Lagrangian derivative (3.17). As shown in figure 3, it is reasonably obtained that the results calculated by both approaches agree well with each other.

To reveal the statistical properties of the evolution of the invariants, the p.d.f.s of the rate of change of the invariants are plotted in figure 4. The field of velocity derivatives is more sensitive to the non-Gaussian nature of turbulence or more generally to its structure, and hence reflects more of its physics (Tsinober 2000). From figure 4, it is interesting to note that the tails of the profiles exhibit approximately -3 power-law change. This property indicates that the large rate of change of the invariant becomes much more probable than the prediction in terms of a Gaussian distribution. Then, according to this property, the p.d.f. (χ) can be approximated as $\text{p.d.f.}(\chi) \sim |\chi|^{-3}$ for large $|\chi|$, where χ represents the rate of change of the invariants. Usually, the

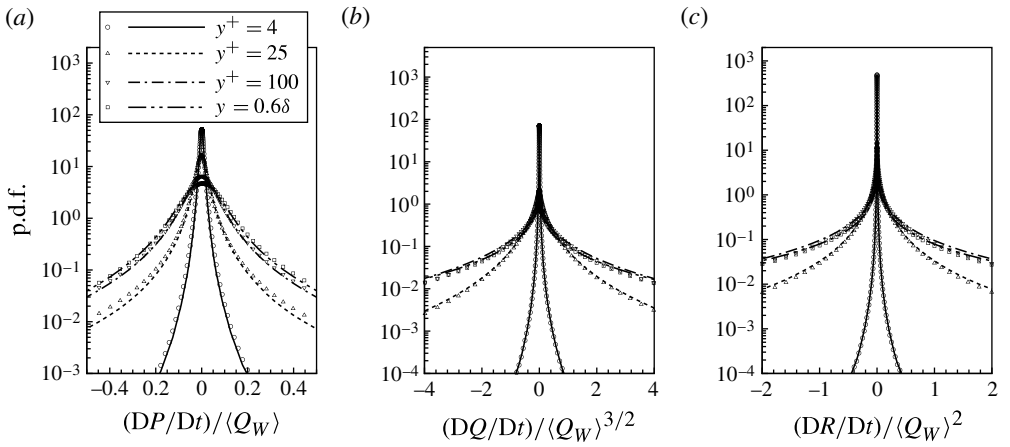

FIGURE 3. Probability density functions of (*a*) $\mathrm{D}P/\mathrm{D}t$, (*b*) $\mathrm{D}Q/\mathrm{D}t$ and (*c*) $\mathrm{D}R/\mathrm{D}t$ at $y^+ = 4$ (full line, circles), $y^+ = 25$ (dashed line, up triangles), $y^+ = 100$ (dash-dotted line, down triangles) and $y = 0.6\delta$ (dash-dot-dot line, squares), corresponding to the viscous sublayer, buffer layer, logarithmic layer and defect layer, respectively. The symbols represent the results obtained by (3.11)–(3.13) and the lines by (3.17).

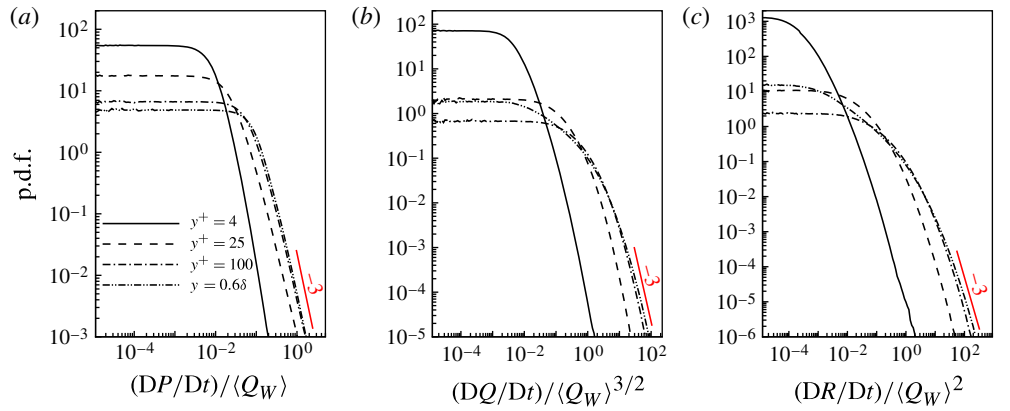

FIGURE 4. (Colour online) Probability density functions of (*a*) $\mathrm{D}P/\mathrm{D}t$, (*b*) $\mathrm{D}Q/\mathrm{D}t$, and (*c*) $\mathrm{D}R/\mathrm{D}t$ at $y^+ = 4$, 25, 100 and $y = 0.6\delta$ with the data taken from the regions with positive material derivatives of invariants.

stochastic term is specified to be Gaussian for modelling the Lagrangian dynamics of the VGT (Meneveau 2011). Therefore, this p.d.f. behaviour can be useful to assess the stochastic term's character and to improve the relevant modelling of turbulence (Girimaji & Pope 1990; Chertkov *et al.* 1999; Chevillard & Meneveau 2006).

Furthermore, it is identified from figure 3 that the p.d.f.s of the rate of change of the invariants in the logarithmic layer are consistent with those in the defect layer, indicating the similar local topological evolutions in the logarithmic layer and defect layer. In the following analysis, we will mainly discuss the results of the logarithmic layer in the outer layer. Moreover, the rate of change of the invariants in the viscous sublayer becomes obviously weak with respect to the other regions, indicating that

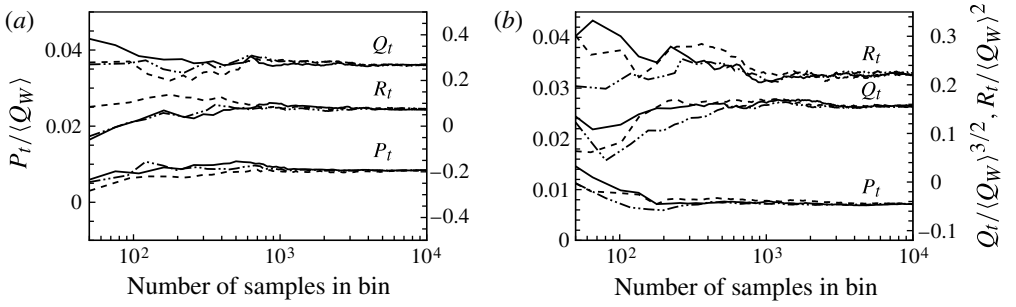

FIGURE 5. The convergence of the statistics of $P_t/\langle Q_W\rangle$, $Q_t/\langle Q_W\rangle^{3/2}$ and $R_t/\langle Q_W\rangle^2$ for (*a*) the buffer layer and (*b*) the logarithmic layer at point (0.0, 1.5, −0.5) in the *P*–*Q*–*R* space. Bin 1: 0.004 × 0.1 × 0.01 (solid line); bin 2: 0.004 × 0.05 × 0.02 (dashed line); bin 3: 0.002 × 0.1 × 0.02 (dash-dot-dot line).

the local flow topologies are clustered near the origin in the normalized *P*–*Q*–*R* space. This leads to a lack of enough samples for dealing with the topological evolution of the viscous sublayer. Thus, the results of the buffer layer are mainly discussed in the inner layer.

4.2. *Conditional mean trajectory*

The Lagrangian evolution of the invariants of the VGT is studied in terms of CMTs by integrating from the conditional mean rate of change of invariants (Martín *et al.* 1998; Ooi *et al.* 1999). These trajectories can be used to reveal the physical mechanisms of the mean Lagrangian evolution of local flow topologies, and are therefore of significance in understanding and modelling the dynamics of structures in turbulent flow. The averaging procedure is similar to the treatment in an incompressible turbulent flow (Ooi *et al.* 1999) and is described by

$$P_t(R_0, Q_0, P_0) = \left\langle \frac{\mathrm{D}P}{\mathrm{D}t} \middle| -\frac{1}{2} \leqslant \frac{P-P_0}{\Delta P}, \frac{Q-Q_0}{\Delta Q}, \frac{R-R_0}{\Delta R} < \frac{1}{2} \right\rangle, \tag{4.1a}$$

$$Q_t(R_0, Q_0, P_0) = \left\langle \frac{\mathrm{D}Q}{\mathrm{D}t} \middle| -\frac{1}{2} \leqslant \frac{P-P_0}{\Delta P}, \frac{Q-Q_0}{\Delta Q}, \frac{R-R_0}{\Delta R} < \frac{1}{2} \right\rangle, \tag{4.1b}$$

$$R_t(R_0, Q_0, P_0) = \left\langle \frac{\mathrm{D}R}{\mathrm{D}t} \middle| -\frac{1}{2} \leqslant \frac{P-P_0}{\Delta P}, \frac{Q-Q_0}{\Delta Q}, \frac{R-R_0}{\Delta R} < \frac{1}{2} \right\rangle, \tag{4.1c}$$

where P_0, Q_0 and R_0 are the bin centres, respectively, and ΔP, ΔQ and ΔR denote the corresponding bin sizes over which the material derivatives are averaged. The expression (4.1) gives the conditional mean rate of change of the invariants at each point in the *P*–*Q*–*R* space, denoting a conditional mean vector field (P_t, Q_t, R_t). The vector field is then used to obtain the CMT, which represents the mean path followed by a point in the *P*–*Q*–*R* space as it evolves temporally.

The bin size is related to the computational resolution of the conditional mean vector quantities. To verify the statistical convergence of the conditional mean vector field, three typical different bins have been examined. The evolutions of P_t, Q_t and R_t at point (0.0, 1.5, −0.5) versus the number of samples per bin in the *P*–*Q*–*R* space are shown in figure 5(*a*,*b*) for the buffer layer and logarithmic layer, respectively. It is identified that the statistical convergence is ensured as the number is approximately over 1000 samples per bin in the buffer layer and over 3000 samples in

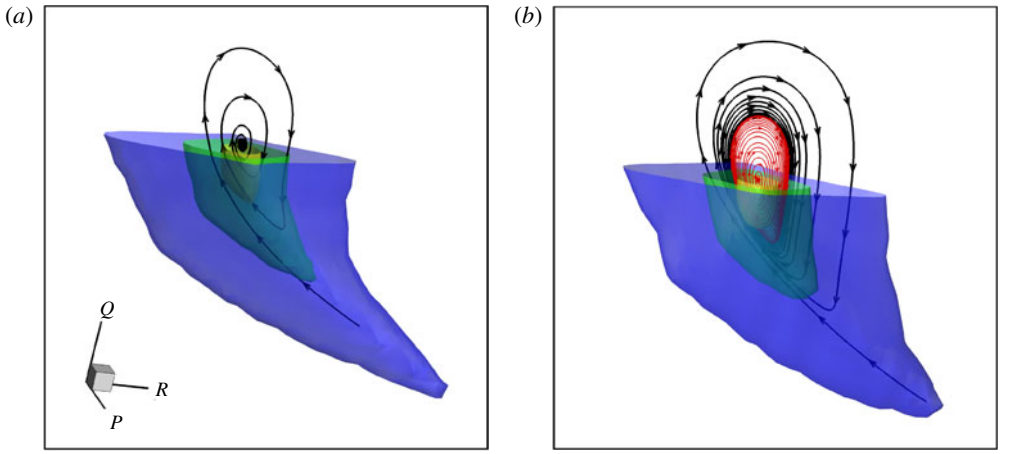

FIGURE 6. The CMTs and isosurfaces of $\mathscr{J}$ for (*a*) the logarithmic layer and (*b*) the buffer layer. The black lines represent the CMTs spiralling inward and the red lines the CMT spiralling outward. The blue, green and yellow isosurfaces denote $\mathscr{J} = 10^{-3}$, 10^{-2} and 10^{-1}, respectively.

the logarithmic layer. In the present study, we have used more than 6000 samples per bin to perform the statistical analysis.

Figure 6 shows the CMTs and isosurfaces of the joint p.d.f.s of the invariants in the normalized *P*–*Q*–*R* space. The joint p.d.f., normalized by its maximum value in the *P*–*Q*–*R* space, is represented by $\mathscr{J}$ for convenience. It is needed to indicate that the point (0.0, 1.5, −0.5) used in figure 5 lays out of the region ($\mathscr{J} > 10^{-3}$) illustrated in figure 6. It means that the sample number per bin for the region in figure 6 is larger than the sample number at the point. As a consequence, the statistical convergence is ensured for the entire *P*–*Q*–*R* space. It is seen that the trajectories near the origin for a weak gradient in the *P*–*Q*–*R* space are well resolved. In the logarithmic layer, the trajectory orbits around the origin and spirals inward, marked by the black line in figure 6(*a*), consistent with the finding of Elsinga & Marusic (2010) in the *Q*–*R* plane for an incompressible boundary layer. In the buffer layer, it is interesting to note that a limit cycle behaviour is illustrated for $10^{-2} < \mathscr{J} < 10^{-1}$ in figure 6(*b*). This feature confirms the result of Mizuno *et al.* (2011) for incompressible turbulent flow. The trajectory (coloured by black) outside the limit cycle spirals inward along the trajectory, while the trajectory (coloured by red) inside the limit cycle spirals outward along the trajectory. Moreover, the relevant evidence that the CMTs are representative of Lagrangian trajectories in the *Q*–*R* plane has also been provided by Chong *et al.* (1998) for wall-bounded incompressible turbulent flow, and flow topology can be directly inferred by the local values of the invariants on the trajectory (Chong *et al.* 1990). So, it is revealed that on average the local topology of fluid particles will change from unstable node/saddle/saddle (UN/S/S) to stable node/saddle/saddle (SN/S/S), to stable focus stretching (SFS), to stable focus compressing (SFC), to unstable focus compressing (UFC) and to UN/S/S.

To analyse the mean evolution time scales of flow topology, the values of *P*, *Q* and *R* along the trajectories for the logarithmic and buffer layers are plotted versus integration time in figure 7. Moreover, to assess the effect of bin size on the resolution of the CMT, the CMTs are calculated by means of bins 1–3. It is seen from figure 7

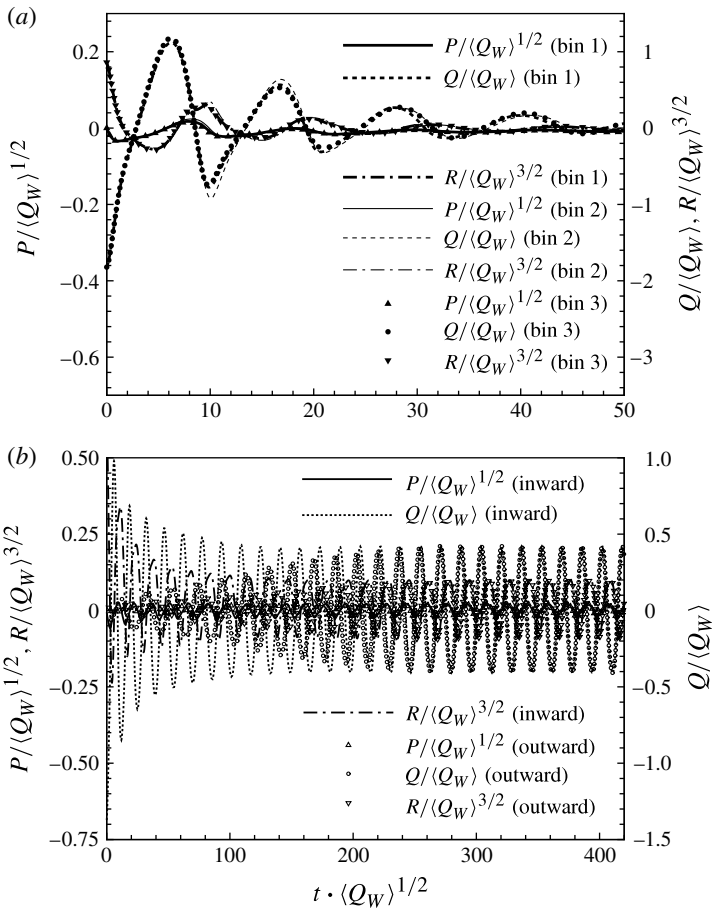

FIGURE 7. Time evolution of P, Q and R along the CMTs for (*a*) the logarithmic layer and (*b*) the buffer layer. The parameters of bins 1–3 are given in the caption of figure 5.

that all trajectories almost collapse, indicating that the bins used can reliably obtain the converged results. In the logarithmic layer, each invariant in figure 7(*a*) decreases with time along the trajectories and approaches zero finally. The period of each orbit is identified to be nearly constant as $11.3\langle Q_W\rangle^{-1/2}$, corresponding to $8.8\delta/U_\infty$ in terms of the outer time scale. In the buffer layer, each invariant in figure 7(*b*) decreases along the inward-spiralling trajectory or increases along the outward-spiralling trajectory, and ultimately converges towards the limit cycle as illustrated in figure 6(*b*). The period of the limit cycle is $16.4\langle Q_W\rangle^{-1/2}$, corresponding to $83\nu_w/u_\tau^2$ in terms of the inner time scale and to $6.0\delta/U_\infty$ in terms of the outer time scale. The periods are regarded as a characteristic time for the life cycle of large-scale structures in the outer and inner layers (Elsinga & Marusic 2010; Atkinson *et al.* 2012). In the outer layer, the period of the orbit is related to the very large-scale coherent structures as discussed in incompressible turbulent boundary layers (Elsinga & Marusic 2010; Atkinson *et al.* 2012). The mean convective velocity in the outer layer of the supersonic turbulent boundary layer is obtained as $\sim 0.9U_\infty$ (Smits *et al.* 1989). Then, the wavelength based on the orbit period $8.8\delta/U_\infty$ in the outer layer is determined

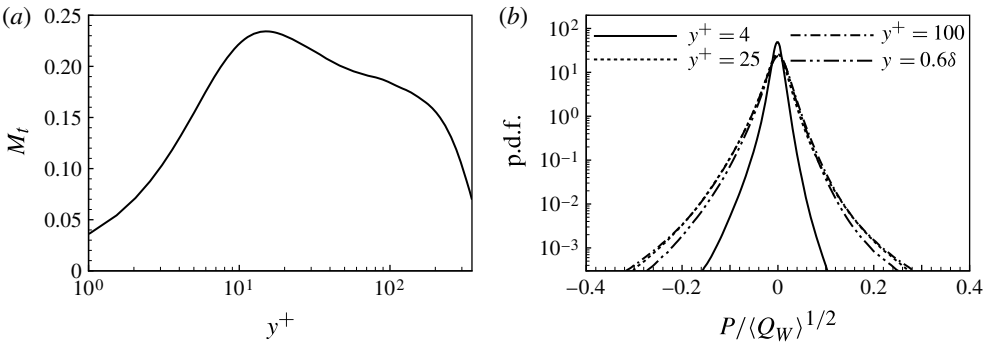

FIGURE 8. (*a*) Distribution of turbulence Mach number along the wall-normal direction and (*b*) p.d.f. of the dilatation at four wall-normal locations.

as 7.92δ, which also corresponds to the scale of very large-scale coherent structures in the outer layer obtained by Ganapathisubramani, Clemens & Dolling (2006). They have experimentally investigated the very large-scale coherent structures for a turbulent boundary layer at Mach 2 and identified that the very large-scale coherent structures have the scale $\sim 8\delta$ in the outer layer based on a low-pass-filtered velocity field.

The mean percentage of the orbit period spent in each topology is calculated by the phase average of time spent in the topology along the trajectories illustrated in figure 7. The percentage of time spent as SFS is 38 % in the buffer layer and 25 % in the logarithmic layer, whereas UFC occupies approximately 25 % in both regions. The percentage of time spent as UN/S/S increases from 32 % in the buffer layer to 42 % in the logarithmic layer, and prevails over SN/S/S which occupies 4 % in the buffer layer and 7 % in the logarithmic layer. Therefore, the fluid particles in the buffer layer spend a greater percentage of time as focal structures with a bias towards SFS. In the logarithmic layer the time spent as focal structures is almost equal to that as non-focal structures, which is similar to homogeneous isotropic turbulence (Martín *et al.* 1998). Moreover, the time spent in the other topologies is less than 1 % because the trajectories are integrated from weak gradient regions.

From the preceding analysis, the mean topological evolution can be viewed as the ensemble average of topological evolutions of individual particle with the same initially selected values of the invariants. It is demonstrated that all possible topologies can develop from the points on the trajectories (Elsinga & Marusic 2010). Most particles in the flow are therefore clustered near the origin of the space of invariants whether the flow topology evolves towards the origin in the logarithmic layer or the limit cycle in the buffer layer on average.

4.3. *Dynamics of mean topological evolution*

To investigate the compressibility effect on the mean topological evolution, we first analyse the compressibility across the boundary layer in terms of the turbulence Mach number M_t and the p.d.f. of dilatation. Figure 8(*a*) shows the distribution of M_t along the wall-normal direction. It is identified that the peak value of M_t is 0.235. We should indicate that the turbulence Mach number of supersonic turbulent boundary layers is generally less than 0.4 even for compressible boundary layer at Mach 8 (e.g. Duan *et al.* 2011). Comparatively, the turbulence Mach number of isotropic compressible turbulence has been considered usually by $M_t \sim 1$, see for example

the recent work on isotropic compressible turbulence investigated by Wang *et al.* (2012) for $M_t = 1$–1.03. The influence of compressibility on dynamics and structures is extremely weak in isotropic compressible turbulence for $M_t < 0.2$ (Pirozzoli & Grasso 2004). However, the compressibility effects of the turbulent boundary layer for $M_t \sim 0.2$ become important and, for example, have been investigated recently by Wang & Lu (2012). Further, the p.d.f.s of the dilatation ($\vartheta = -P$) are examined and exhibited in figure 8(*b*). It is seen that the profiles are more skewed to the $P < 0$ domain.

Owing to the complexity of the 3D CMTs in the normalized P–Q–R space, it is convenient to exhibit the mean topological evolution in the Q–R plane for selected values of P (Suman & Girimaji 2009, 2010; Wang & Lu 2012). To clarify the compressibility effect, the mean topological evolution is analysed for the $P > 0$ (or compressed) and $P < 0$ (or expanding) regions, respectively. For comparison, the statistical quantities in the 'incompressible' region with P around zero are discussed. Based on the p.d.f.s of the dilatation in figure 8(*b*), we choose three typical values of $P\langle Q_W\rangle^{-1/2}$ as -0.1, 0 and 0.1 to classify the corresponding regions.

The evolution of local flow topology in the 'incompressible' region is obtained using conditional statistics upon zero dilatation or $|P\langle Q_W\rangle^{-1/2}| < \varepsilon$, where ε is a threshold value. To obtain the meaningful results in the 'incompressible' region, we have chosen ε as 0.001 which corresponds to the half-bin size of ΔP as shown in figures 5 and 7 for the convergent examinations. The conditional mean terms in (3.11)–(3.13) in the buffer layer are then obtained and shown in figure 9 by use of their vectors and contours for demonstration. From figure 9(*a*), the local topology of fluid particles changes around the origin in a clockwise direction from SFS to UFC, UN/S/S and SN/S/S topology in the Q–R plane, consistent with the topology evolution of incompressible turbulent flows (Chong *et al.* 1998; Martín *et al.* 1998; Ooi *et al.* 1999; Elsinga & Marusic 2010; Bermejo-Moreno *et al.* 2010; Atkinson *et al.* 2012). The magnitude of the mean rate of change of the Q and R (proportional to the vector length) increases with increasing distance from the origin. However, along the $R > 0$ part of the null discriminant curve (i.e. $\Delta = 0$) the vector magnitude remains relatively small. These results are consistent with the trends observed from the analysis of incompressible isotropic turbulence (Martín *et al.* 1998; Ooi *et al.* 1999) and incompressible turbulent boundary layers (Elsinga & Marusic 2010).

As $Q = Q_W + Q_S$ and $R = R_S - \omega_i S_{ij} \omega_j/4$, we can understand that Q represents the competition between enstrophy and dissipation, and R the competition between enstrophy production and dissipation production (Chevillard *et al.* 2008; Wang & Lu 2012), where the enstrophy production is associated with the enstrophy amplification due to vortex stretching. The dynamics of Q and R related to the mutual-interaction terms among the invariants are shown in figure 9(*b*). The Q tends to be increased in the enstrophy production dominated region (i.e. $R < 0$) and to be decreased in the dissipation-production-dominated region (i.e. $R > 0$). Such properties are attributed to the vortex stretching and the self-amplification of the strain-rate tensor in (3.14) and (3.16). The amplification of $|Q|$ in the enstrophy- and enstrophy-production-dominated region (i.e. $Q > 0$ and $R < 0$) and the dissipation- and dissipation-production-dominated region (i.e. $Q < 0$ and $R > 0$) can lead to the finite-time singularity of RE dynamics. By comparing with figure 9(*a,b*), it is deduced that the clockwise spiral behaviour of the local flow topology in the Q–R plane mainly originates from the mutual interaction of the invariants. Moreover, the rate of change of R_S due to the mutual interaction is completely balanced by that of $w_i S_{ij} w_j$ in the 'incompressible' region as represented in (3.13).

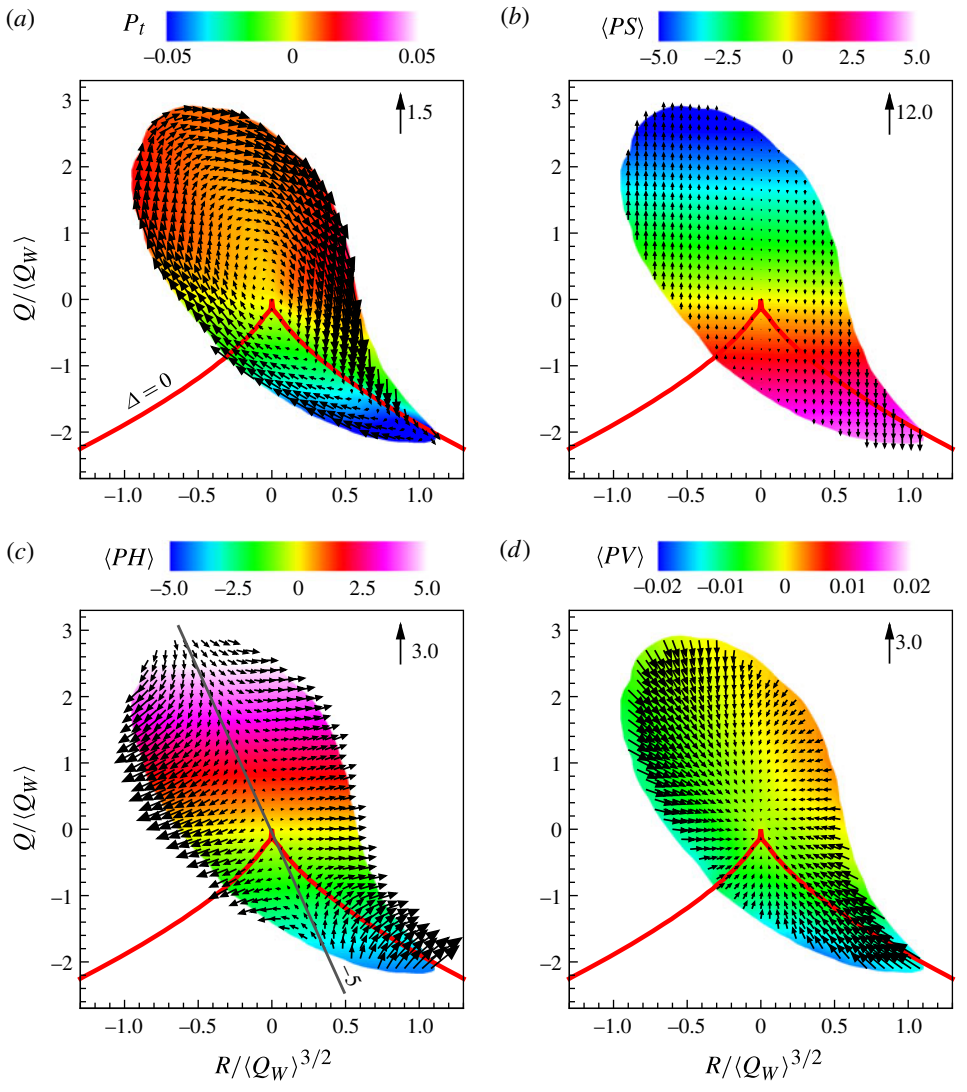

FIGURE 9. Conditional mean terms in (3.11)–(3.13) in the buffer layer by use of the vectors and contours for demonstration in the $P = 0$ plane: (*a*) the total R_t–Q_t (vectors) and P_t (contours); (*b*) the mutual-interaction terms $\langle RS \rangle$–$\langle QS \rangle$ (vectors) and $\langle PS \rangle$ (contours); (*c*) The pressure Hessian terms $\langle RH \rangle$–$\langle QH \rangle$ (vectors) and $\langle PH \rangle$ (contours); (*d*) the viscous terms $\langle RV \rangle$–$\langle QV \rangle$ (vectors) and $\langle PV \rangle$ (contours). The data with $\mathscr{J} < 10^{-4}$ is not shown. The length of the arrow drawn in each figure represents the reference scale in the Q-direction of the vectors. Here P_t, PS, PH and PV are normalized by $\langle Q_W \rangle$, Q_t, QS, QH and QV are normalized by $\langle Q_W \rangle^{3/2}$ and R_t, RS, RH and RV are normalized by $\langle Q_W \rangle^2$.

The dynamics related to the pressure Hessian is shown in figure 9(*c*) and trajectories will move away from an asymptote. The asymptote approaches a straight line with a slope -5 in the normalized Q–R plane, consistent with the shape of the probability distribution for Q and R. The enstrophy production is therefore dominated on the left-hand side of the asymptote and the dissipation production on the right-hand side. On average, the enstrophy production rate tends to be increased in the enstrophy

production region and the dissipation production rate tends to be increased in the dissipation production region. These features reveal that the pressure terms lead to the amplification of $|R|$. Moreover, because the density and pressure gradients are strongly constrained to be almost parallel to each other in this flow, the baroclinic effect (not shown here) becomes very weak.

The dynamics determined by $\langle QV \rangle$ and $\langle RV \rangle$ are shown in figure 9(*d*), indicating that the viscous effect tends to attract trajectories to the origin. It is consistent with the findings in isotropic turbulence (Chevillard *et al.* 2008) and wall-bounded turbulent flows (Mizuno *et al.* 2011). Fluid particles move towards the origin in the Q–R plane in an incompressible turbulent boundary layer with $Re_\theta = 300$ (Chacin & Cantwell 2000). This property is associated with the fact that the Reynolds number is so low that trajectories are handled by the viscous effect. Moreover, Ooi *et al.* (1999) have analysed the combined pressure and viscous effects for incompressible isotropic turbulence in terms of the evolution equations of the invariants and indicated the influence of viscous dissipation in the topological evolution.

It is seen from the contours of P_t in figure 9(*a*) that on average the fluid particles tend to be compressed in the enstrophy dominated region (i.e. $Q > 0$) and to be expanding in the dissipation dominated region (i.e. $Q < 0$), which is attributed to the pressure effect shown in figure 9(*c*). However, the mutual interaction produces an opposite effect on the rate of change of the dilatation. Comparing with figure 9(*b,c*), it is found that the effect of the pressure Hessian tensor PH is balanced primarily by the contribution of Q, with $PS + PH = 0$ for incompressible and inviscid flows. Moreover, the contribution of the viscous term PV is the smallest one as exhibited in figure 9(*d*).

Figure 10 exhibits the corresponding conditional mean terms in (3.11)–(3.13) in the 'incompressible' region for the logarithmic layer. Compared with the counterpart for the buffer layer as discussed above, it is identified that the dynamics characters in the logarithmic layer becomes stronger with respect to the buffer layer, which is also observed from figure 3. In particular, as shown in figures 9(*c*) and 10(*c*), the slope of the asymptote changes from -5 to -3.6 in the normalized Q–R plane due to the change of mean shear. This behaviour is associated with the change of probability distribution for Q and R, which appears to be more elongated in the buffer layer than in the logarithmic layer.

The mean topological evolution of fluid particles in the locally compressed and expanding regions is obtained using conditional statistics for $P\langle Q_W \rangle^{-1/2} = 0.1$ and -0.1, and is illustrated in figures 11 and 12 for the buffer layer, respectively. As shown in figures 11(*a*) and 12(*a*), Q tends to be decreased and R tends to be increased in the locally compressed region, and Q tends to be increased and R tends to be decreased in the locally expanding region. These behaviours are consistent with the findings that the enstrophy production tends to be decreased in the locally compressed region and to be increased in the locally expanding region (Wang & Lu 2012). The magnitude of the mean rate of change of the Q and R increases with the decrease in Q or Δ.

The local topological evolution in the Q–R plane is considered. On average, the local topology of fluid particles in the locally compressed region changes from SFS to SFC to UFC to UN/S/S or from SFS to SN/S/S to UN/S/S. While the local topology of fluid particles in the locally expanding region changes from UN/S/S to SFS and unstable focus stretching (UFS) through SN/S/S and UFC, respectively. Moreover, the Lagrangian evolution of P in the compressed and expanding regions are similar to that in the 'incompressible' region. Therefore, the topological evolution in the P–Q–R

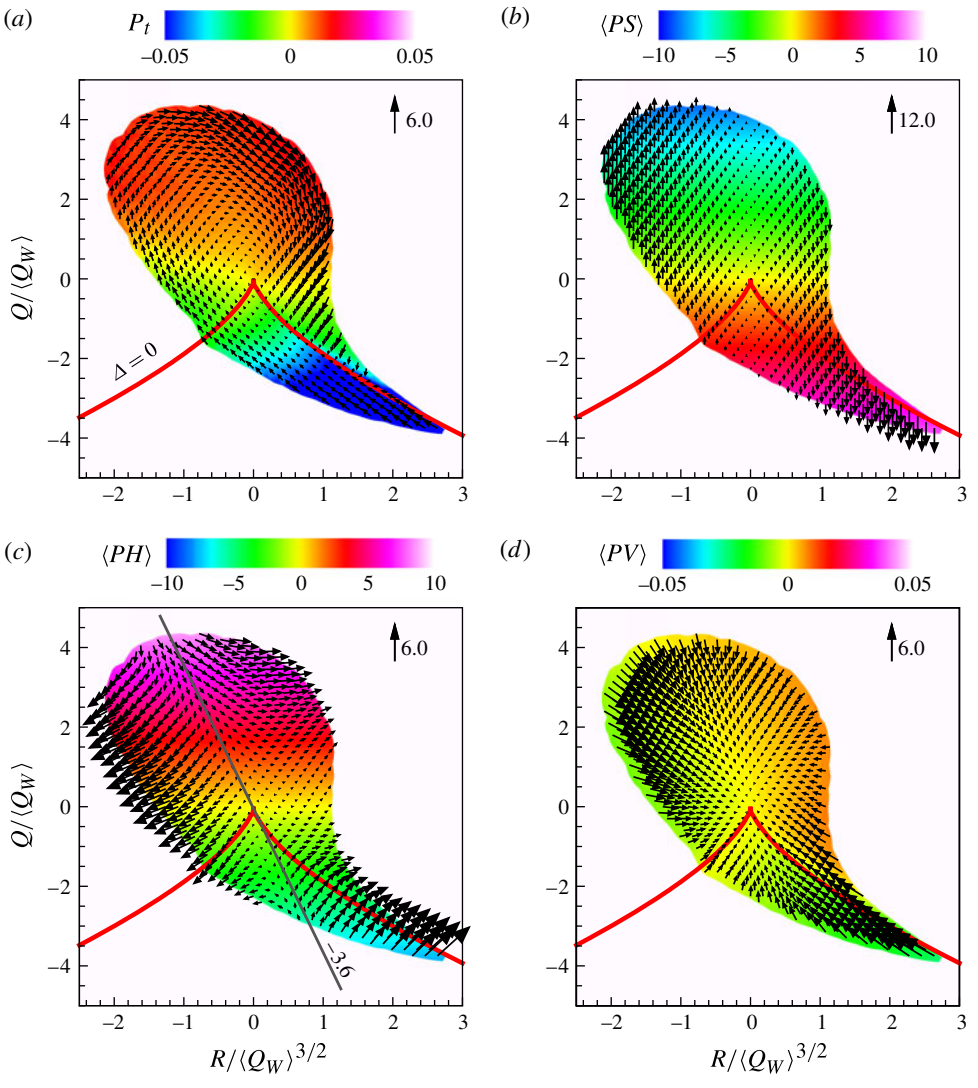

FIGURE 10. Conditional mean terms in (3.11)–(3.13) in the logarithmic layer by use of the vectors and contours for demonstration in the $P = 0$ plane. For other details see figure 9.

space can in general be described as follows. On average, fluid particles move spirally from $Q > 0$ and $R < 0$ to $Q < 0$ and $R > 0$ in the region of $P > 0$, from $P > 0$ to $P < 0$ in the region of $Q < 0$, from $Q < 0$ and $R > 0$ to $Q > 0$ and $R < 0$ in the region of $P < 0$. Correspondingly, the local topology of fluid particles near the limit cycle in the buffer layer will change from UN/S/S to SN/S/S to SFS in the locally expanding region, while from SFS to SFC to UFC to UN/S/S in the locally compressed region.

Comparing with the results shown in figures 9(*b*), 11(*b*) and 12(*b*), it is found that the compressibility effect on the contribution of the mutual interaction to topological evolution is relatively weak. However, it is clearly seen from (3.11)–(3.13) that P^2, PQ and PR are involved into the mutual-interaction terms PS, QS and RS, respectively, for compressible flows. Therefore, compared with the 'incompressible' region, these terms

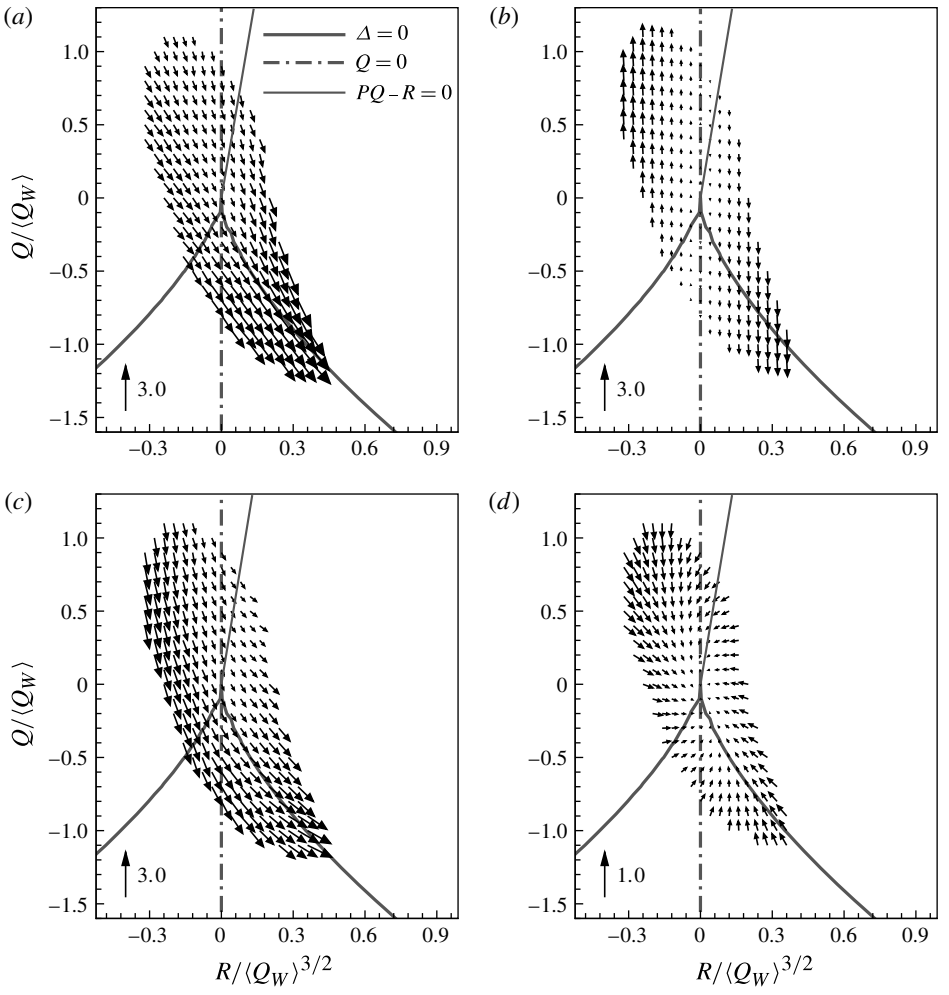

FIGURE 11. Conditional mean terms in (3.11)–(3.13) in the buffer layer by use of the vectors and contours for demonstration in the $P\langle Q_W \rangle^{-1/2} = 0.1$ plane. For other details see figure 9.

tend to amplify the magnitude of the rate of change of the invariants in the locally compressed region and to reduce the magnitude in the locally expanding region.

To quantitatively demonstrate the effect of Mach number on the mutual-interaction terms, we typically consider the term PR in the evolution equation (3.13) of the third invariant R. The contribution of PR to the rate of change of $\mathrm{D}R/\mathrm{D}t$ in compressible turbulent boundary layers at $Ma = 2$ and 4.9 is shown in figure 13. Noted that the opposite tendencies in the locally compressed ($P > 0$) and expanding ($P < 0$) regions occur for $\mathrm{D}R/\mathrm{D}t$, as shown in figures 11(a) and 12(a). Therefore, the rate of change of R is analysed statistically in two different regions, i.e. locally compressed and expanding regions. Moreover, it is deduced from the definition of the term PR that the values of PR in the enstrophy-production-dominated ($R < 0$) and dissipation-production-dominated ($R > 0$) regions mainly cancel each other in locally compressed or expanding regions. To reveal the contribution of PR to the rate of change of R

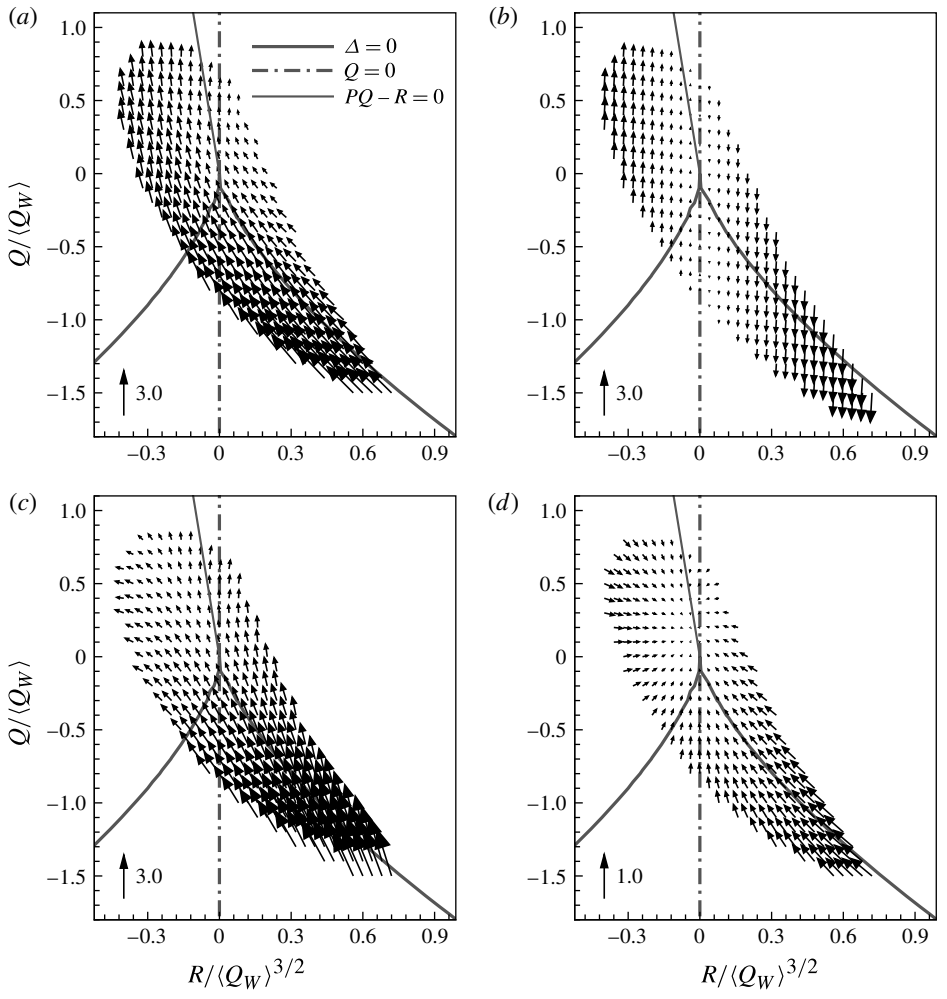

FIGURE 12. Conditional mean terms in (3.11)–(3.13) in the buffer layer by use of the vectors and contours for demonstration in the $P\langle Q_W \rangle^{-1/2} = -0.1$ plane. For other details see figure 11.

in the invariants space for the two Mach numbers, the term PR is analysed in four regions shown in figure 13. It is seen that the contributions of PR to the rate of change of R in compressible turbulent boundary layers at $Ma = 2$ and 4.9 are qualitatively similar, but with different values.

As shown in figure 13(a), the mean value of $\mathrm{D}R/\mathrm{D}t$ in the locally compressed region is positive due to the fact that the term PR in the region of $P > 0$ and $R > 0$ is positive definite, which is consistent with the results of figure 11(a). Therefore, the term PR in the region of $P > 0$ and $R > 0$ makes a positive contribution to the magnitude of $\langle \mathrm{D}R/\mathrm{D}t | P > 0 \rangle$, and the term in the region of $P > 0$ and $R < 0$ makes a negative contribution. In contrast, the mean values of $\mathrm{D}R/\mathrm{D}t$ in the locally expanding region is negative as shown in figure 12(a). The term PR in the region of $P < 0$ and $R > 0$ makes a positive contribution to the magnitude of $\langle \mathrm{D}R/\mathrm{D}t | P < 0 \rangle$, and the term

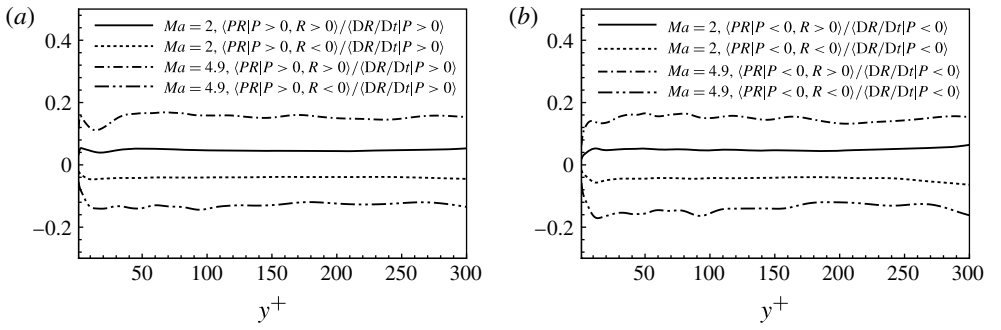

FIGURE 13. Distributions of conditional average PR in the regions of (a) $P > 0$ and (b) $P < 0$ in compressible turbulent boundary layers at $Ma = 2$ and 4.9.

in the region of $P > 0$ and $R < 0$ makes a negative contribution shown in figure 13(b). Furthermore, the contribution rate of PR to the rate of change of R is about 4 % at $Ma = 2$. With the increase of Mach number, the occurrence probabilities of fluid particles in the strongly expanding and compressed regions increases (Lagha *et al.* 2011) and the contribution rate of PR increases to about 15 % at $Ma = 4.9$.

The behaviours related to the pressure Hessian in the locally compressed and expanding regions are shown in figures 11(c) and 12(c), respectively. The pressure Hessian terms have a dominant influence on the topological evolution with respect to the other terms. The opposite tendencies in the locally compressed and expanding regions occur for the topological evolution. It is deduced that the pressure effect tends to strengthen the dissipation in the locally compressed region and to reduce the dissipation in the locally expanding region. Unlike the behaviour in the 'incompressible' region, the pressure effect on the flow topological evolution in the locally compressed and expanding regions is mainly dependent of P and almost independent of Q and R. These behaviours imply the complexity of modelling the pressure Hessian for compressible turbulence. Moreover, to investigate the difference between $\langle Q_W\rangle$ and A^2 normalization in locally expanding and compressed regions, figure 14 shows the joint p.d.f. of P and the pressure Hessian term QH based on the two normalizations in the buffer layer. Similar to the results obtained by $\langle Q_W\rangle$ normalization, the term QH/A^3 tends to be positive in the expanding region and to be negative in the compressed region. This behaviour is also clearly presented by the average of QH/A^3 conditioned on P/A and is consistent with the results of figures 11(c) and 12(c). Therefore, the relevant results on compressibility effects in terms of the $\langle Q_W\rangle$ normalization is qualitatively similar to those in terms of the A^2 normalization.

To investigate the pressure effect on $\omega_i S_{ij}\omega_j$ which is referred to as vortex stretching (Tsinober 2009), figure 15(a) shows the wall-normal distribution of the volume fraction of the enstrophy production region ($\omega_i S_{ij}\omega_j > 0$) and the enstrophy destruction region ($\omega_i S_{ij}\omega_j < 0$), where the enstrophy destruction is associated with the enstrophy decay due to vortex contraction. It confirms the fact that enstrophy production prevails over enstrophy destruction (Taylor 1938). The volume fraction of the vortex stretching region is almost equal to that of the vortex contraction region in the viscous sublayer, increases gradually in the buffer layer, levels off at around 3/4 in the logarithmic layer and decreases in the defect layer. The Lagrangian evolution equation of $\omega_i S_{ij}\omega_j$

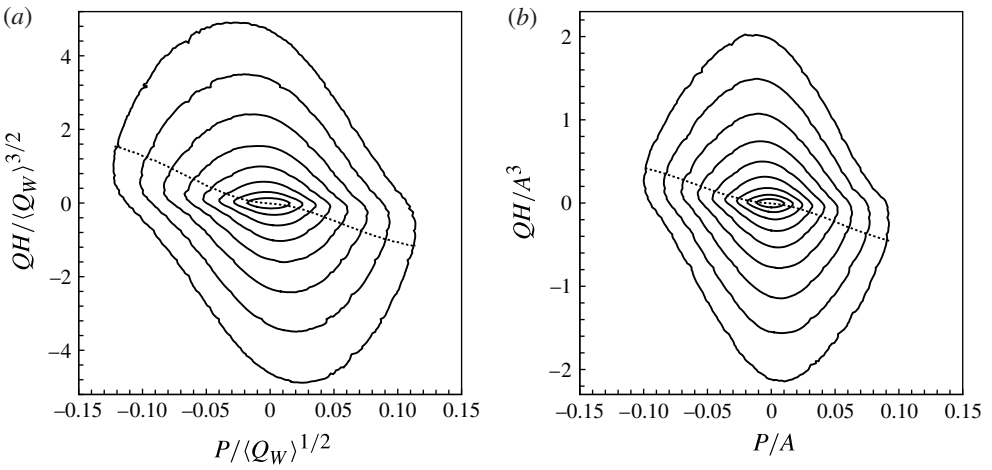

FIGURE 14. Joint p.d.f.s of (*a*) $P/\langle Q_W\rangle^{1/2}$ and $QH/\langle Q_W\rangle^{3/2}$ and (*b*) P/A and QH/A^3 on a logarithmic scale in the buffer layer. The outer contour level is -4 and the inner contour level is -0.5. The increment of contours is 0.5. The dashed lines denote the average of the normalized QH conditioned on the normalized P.

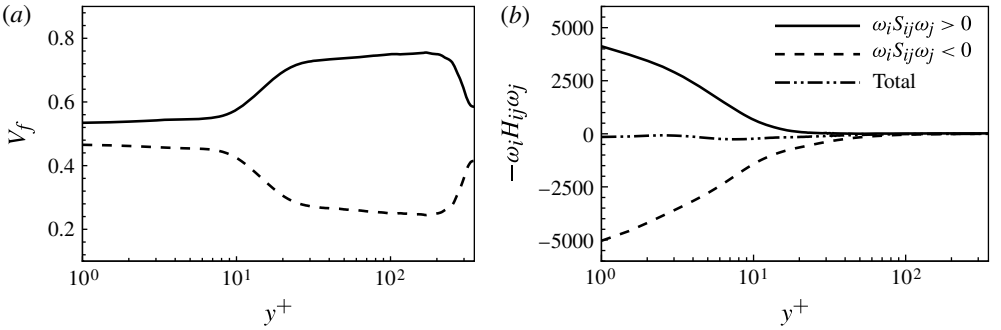

FIGURE 15. The distributions of (*a*) the volume fraction V_f of $\omega_i S_{ij}\omega_j > 0$ and $\omega_i S_{ij}\omega_j < 0$ and (*b*) $-\omega_i H_{ij}\omega_j$ along the wall-normal direction.

is given by

$$\frac{\mathrm{D}(\omega_i S_{ij}\omega_j)}{\mathrm{D}t} = -4\left(P^2 Q_W + 2Q_S Q_W - 2P(\boldsymbol{S}:\boldsymbol{W}^2) - \boldsymbol{S}^2:\boldsymbol{W}^2\right) - \omega_i H_{ij}\omega_j + 4\left(P(\boldsymbol{W}:\boldsymbol{B}) - Q_W \mathrm{tr}(\boldsymbol{B}) + (2\boldsymbol{S}\cdot\boldsymbol{W} - \boldsymbol{W}^2):\boldsymbol{B}\right) - 4\left(P(\boldsymbol{W}:\boldsymbol{V}) - Q_W \mathrm{tr}(\boldsymbol{V}) + (2\boldsymbol{S}\cdot\boldsymbol{W} - \boldsymbol{W}^2):\boldsymbol{V}\right). \tag{4.2}$$

The pressure effect on the evolution of $\omega_i S_{ij}\omega_j$ is measured by $-\omega_i H_{ij}\omega_j$, which has been discussed in incompressible flows (Ooi *et al.* 1999; Tsinober 2009). It is seen from (3.14) and (3.16) that, unlike the dissipation, the enstrophy is not directly associated with the pressure. The pressure affects the enstrophy by means of $\omega_i S_{ij}\omega_j$ as given in (3.14) and (4.2). Figure 15(*b*) shows the wall-normal distribution of $\omega_i H_{ij}\omega_j$ for the enstrophy production and destruction regions. The pressure contribution to the rate of change of $\omega_i S_{ij}\omega_j$ in the enstrophy production region attains a large value

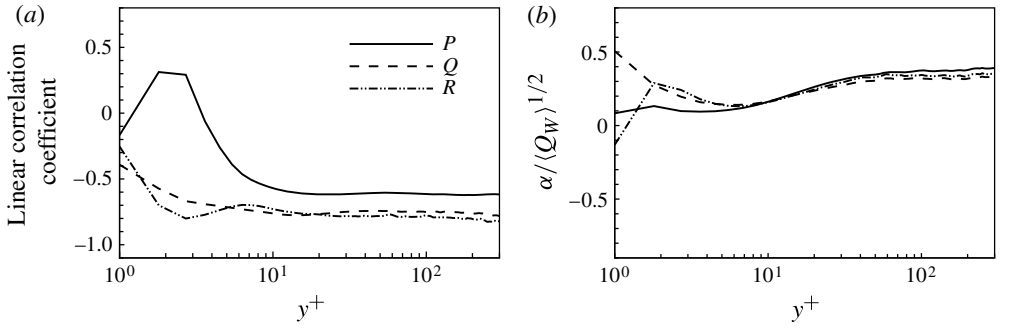

FIGURE 16. The distributions of (*a*) linear correlation coefficients and (*b*) regression coefficients.

in the viscous sublayer and then decreases with the increase in y^+ as well as is opposite to the contribution in the enstrophy destruction region. It is thus obtained that the pressure effect plays a role in enhancing the contraction of vortex in the vortex-contraction region and in strengthening the stretching of vortex in the vortex-stretching region.

Furthermore, comparing figures 11(*d*) and 12(*d*) with 9(*d*), it is observed that the contribution to the topological evolution in the locally compressed and expanding regions due to viscous effect is similar to that in the 'incompressible' region. A linear approximation model $\boldsymbol{V} = -\alpha \boldsymbol{A}$ was proposed by Martin *et al.* (1997), where α is the inverse of a characteristic diffusion time scale. Then, the viscous terms in (3.11)–(3.13) are derived as

$$PV = -\alpha P, \quad QV = -2\alpha Q, \quad RV = -3\alpha R. \tag{4.3}$$

To deal with this model, the correlations between the invariants and their rates due to the viscous effect are examined using the linear regression analysis method. Figure 16(*a*) shows the distributions of linear correlation coefficients along the wall-normal direction with nearly constant values of 0.6 for P and 0.8 for Q and R in the outside region of the viscous sublayer, indicating that there exist significant linear correlations between the invariants and the corresponding viscous rates. It is also suggested that the linear damping model is statistically reasonable for modelling the viscous effect of the VGT only in the outside region of the viscous sublayer, which confirms the finding of Chacin & Cantwell (2000). The regression coefficients, representing the inverse of characteristic diffusion time scale, are shown in figure 16(*b*). The discrepancies among them are attributed to the shortcomings of the linear model as indicated by Martin *et al.* (1997). The regression coefficients increase from approximately 0.15–0.35 in the buffer layer and level off in the logarithmic layer and defect layer. The viscous terms attract trajectories to the origin as shown in figures 9–12. Therefore, fluid particles in the logarithmic layer are more likely to move towards the origin in the normalized P–Q–R space. This is responsible for the different behaviours of the topologies of CMTs in the buffer layer and logarithmic layer as shown in figure 6.

5. Concluding remarks

The statistics and dynamics of the local topological evolution of compressible turbulent boundary layers at Mach 2 have been studied in terms of the detailed

analysis of the invariants of the VGT. The main conclusions are briefly summarized as follows.

The p.d.f.s of the rate of change of the invariants exhibit a decrease with the -3 power law in the inner and outer layers. It is helpful to assess and improve the stochastic term in turbulence models. The mean Lagrangian evolution of the invariants of the VGT is derived using CMTs by integrating from conditional mean rate of change of invariants. The trajectories reveal inward-spiralling orbits around and converging to the origin of the P–Q–R space in the logarithmic layer, while they are repelled by the vicinity of the origin and converge towards the limit cycle in the buffer layer. On average, the local topology of fluid particles will change from topology UN/S/S to SN/S/S, to SFS, to SFC, to UFC, and to UN/S/S. The difference in the mean topological evolution between the logarithmic and buffer layers is attributed to the viscous effect.

The compressibility effect on the mean topological evolution is investigated for the 'incompressible', compressed and expanding regions. It is found that the mean evolution of flow topologies is altered by the compressibility. The mean evolution of the Q and R in the 'incompressible' region is consistent with that in incompressible turbulent flows. On average fluid particles tend to be compressed in the enstrophy-dominated region and to be expanding in the dissipation-dominated region due to the pressure effect. In the locally compressed region Q tends to be decreased and R tends to be increased, and in the locally expanding region Q tends to be increased and R tends to be decreased. Therefore, the fluid particles move spirally from $Q > 0$ and $R < 0$ to $Q < 0$ and $R > 0$ in the region of $P > 0$, from $P > 0$ to $P < 0$ in the region of $Q < 0$, from $Q < 0$ and $R > 0$ to $Q > 0$ and $R < 0$ in the region of $P < 0$.

The dynamics of topological evolution is investigated based on the analysis of the mutual-interaction terms, pressure Hessian term, baroclinic effect and viscous action. The mutual interaction involves the vortex stretching and self-amplification of the strain-rate tensor and is the root of the clockwise spiral behaviour of the local flow topology in the Q–R plane. The baroclinic effect is weak because the density and pressure gradients are strongly constrained to be almost parallel to each other in this flow. It is revealed that the compressibility effect is mainly related to the pressure Hessian term. The viscous terms lead to the decrease of the invariants due to viscous dissipation. This is why the trajectory always spirals inward in the P–Q–R space for strong gradient region where viscous dissipation is dominant. Moreover, significant challenges still remain to develop models for the pressure Hessian term due to its importance and complexity, especially for compressible turbulent flows.

Acknowledgements

This work was supported by the National Natural Science Foundation of China (Nos 11132010 and 11072236) and the 111 Project (No. B07033).

REFERENCES

ANDREOPOULOS, Y. & HONKAN, A. 2001 An experimental study of the dissipative and vortical motion in turbulent boundary layers. *J. Fluid Mech.* **439**, 131–163.

ATKINSON, C., CHUMAKOV, S., BERMEJO-MORENO, I. & SORIA, J. 2012 Lagrangian evolution of the invariants of the velocity gradient tensor in a turbulent boundary layer. *Phys. Fluids* **24**, 105104.

ATKINSON, C., COUDERT, S., FOUCAUT, J.-M., STANISLAS, M. & SORIA, J. 2011 The accuracy of tomographic particle image velocimetry for measurements of a turbulent boundary layer. *Exp. Fluids* **50**, 1031–1056.

BATCHELOR, G. K. 1967 *An Introduction to Fluid Mechanics*. Cambridge University Press.

BERMEJO-MORENO, I., ATKINSON, C., CHUMAKOV, S., SORIA, J. & WU, X. 2010 Flow topology and non-local geometry of structures in a flat-plate turbulent boundary layer. In *Proceedings of the Summer Program*. Centre for Turbulence Research, Stanford University.

BLACKBURN, H. M., MANSOUR, N. N. & CANTWELL, B. J. 1996 Topology of fine-scale motions in turbulent channel flow. *J. Fluid Mech.* **310**, 269–292.

CANTWELL, B. J. 1992 Exact solution of a restricted Euler equation for the velocity gradient tensor. *Phys. Fluids* A **4** (4), 782–793.

CHACIN, J. M. & CANTWELL, B. J. 2000 Dynamics of a low Reynolds number turbulent boundary layer. *J. Fluid Mech.* **404**, 87–115.

CHEN, J. H., CHONG, M. S., SORIA, J., SONDERGAARD, R., PERRY, A. E., ROGERS, M., MOSER, R. & CANTWELL, B. J. 1990 A study of the topology of dissipating motions in direct numerical simulations of time-developing compressible and incompressible mixing layers. In *Proceedings of the Summer Program*. Centre for Turbulence Research, Stanford University.

CHERTKOV, M., PUMIR, A. & SHRAIMAN, B. I. 1999 Lagrangian tetrad dynamics and the phenomenology of turbulence. *Phys. Fluids* **11** (8), 2394–2410.

CHEVILLARD, L. & MENEVEAU, C. 2006 Lagrangian dynamics and statistical geometric structure of turbulence. *Phys. Rev. Lett.* **97**, 174501.

CHEVILLARD, L., MENEVEAU, C., BIFERALE, L. & TOSCHI, F. 2008 Modelling the pressure Hessian and viscous Laplacian in turbulence: comparisons with direct numerical simulation and implications on velocity gradient dynamics. *Phys. Fluids* **20**, 101504.

CHONG, M. S., PERRY, A. E. & CANTWELL, B. J. 1990 A general classification of three-dimensional flow fields. *Phys. Fluids* A **2** (5), 765–777.

CHONG, M. S., SORIA, J., PERRY, A. E., CHACIN, J., CANTWELL, B. J. & NA, Y. 1998 Turbulence structures of wall-bounded shear flows found using DNS data. *J. Fluid Mech.* **357**, 225–247.

CHU, Y.-B. 2013 Numerical investigations of shock–shock interaction and supersonic turbulent boundary layer. PhD thesis, University of Science and Technology of China, Hefei.

DUAN, L., BEEKMAN, I. & MARTÍN, M. P. 2011 Direct numerical simulation of hypersonic turbulent boundary layers. Part 3. Effect of Mach number. *J. Fluid Mech.* **672**, 245–267.

ELSINGA, G. E. & MARUSIC, I. 2010 Evolution and lifetimes of flow topology in a turbulent boundary layer. *Phys. Fluids* **22**, 015102.

FRISCH, U. 1995 *Turbulence*. Cambridge University Press.

GANAPATHISUBRAMANI, B., CLEMENS, N. T. & DOLLING, D. S. 2006 Large-scale motions in a supersonic turbulent boundary layer. *J. Fluid Mech.* **556**, 271–282.

GIRIMAJI, S. S. & POPE, S. B. 1990 A diffusion model for velocity gradients in turbulence. *Phys. Fluids* A **2** (2), 242–256.

JEONG, E. & GIRIMAJI, S. S. 2003 Velocity-gradient dynamics in turbulence: effect of viscosity and forcing. *Theor. Comput. Fluid Dyn.* **16**, 421–432.

JIANG, G. S. & SHU, C. W. 1996 Efficient implementation of weighted ENO schemes. *J. Comput. Phys.* **126**, 202–228.

KIM, J., MOIN, P. & MOSER, R. 1987 Turbulence statistics in fully developed channel flow at low Reynolds number. *J. Fluid Mech.* **177**, 133–166.

LAGHA, M., KIM, J., ELDREDGE, J. D. & ZHONG, X. 2011 A numerical study of compressible turbulent boundary layers. *Phys. Fluids* **23**, 015106.

LEE, K., GIRIMAJI, S. S. & KERIMO, J. 2009 Effect of compressibility on turbulent velocity gradients and small-scale structure. *J. Turbul.* **10** (9), 1–18.

LI, Y., CHEVILLARD, L., EYINK, G. & MENEVEAU, C. 2009 Matrix exponential-based closures for the turbulent subgrid-scale stress tensor. *Phys. Rev.* E **79**, 016305.

LÜTHI, B., HOLZNER, M. & TSINOBER, A. 2009 Expanding the Q–R space to three dimensions. *J. Fluid Mech.* **641**, 497–507.

MARTÍN, J., OOI, A., CHONG, M. S. & SORIA, J. 1998 Dynamics of the velocity gradient tensor invariants in isotropic turbulence. *Phys. Fluids* **10** (8), 2336–2346.

MARTIN, J., OOI, A., DOPAZO, C., CHONG, M. S. & SORIA, J. 1997 The inverse diffusion time scale of velocity gradients in homogeneous isotropic turbulence. *Phys. Fluids* **9** (4), 814–816.

MENEVEAU, C. 2011 Lagrangian dynamics and models of the velocity gradient tensor in turbulent flows. *Annu. Rev. Fluid Mech.* **43**, 219–245.

MIZUNO, Y., ATKINSON, C. & SORIA, J. 2011 Topology and dynamics of flow structures in wall-bounded turbulent flows. *J. Phys.: Conf. Ser.* **318**, 062018.

OOI, A., MARTIN, J., SORIA, J. & CHONG, M. S. 1999 A study of the evolution and characteristics of the invariants of the velocity-gradient tensor in isotropic turbulence. *J. Fluid Mech.* **381**, 141–174.

PERRY, A. E. & CHONG, M. S. 1987 A description of eddying motions and flow patterns using critical-point concepts. *Annu. Rev. Fluid Mech.* **19**, 125–155.

PIROZZOLI, S., BERNARDINI, M. & GRASSO, F. 2008 Characterization of coherent vortical structures in a supersonic turbulent boundary layer. *J. Fluid Mech.* **613**, 205–231.

PIROZZOLI, S. & GRASSO, F. 2004 Direct numerical simulations of isotropic compressible turbulence: influence of compressibility on dynamics and structures. *Phys. Fluids* **16** (12), 4386–4407.

PIROZZOLI, S., GRASSO, F. & GATSKI, T. B. 2004 Direct numerical simulation and analysis of a spatially evolving supersonic turbulent boundary layer at $M = 2.25$. *Phys. Fluids* **16** (3), 530–545.

POPE, S. B. 2000 *Turbulent Flows*. Cambridge University Press.

SAGAUT, P. & CAMBON, C. 2008 *Homogeneous Turbulence Dynamics*. Cambridge University Press.

SHU, C. W. & OSHER, S. 1988 Efficient implementation of essentially non-oscillatory shock-capturing schemes. *J. Comput. Phys.* **77**, 439–471.

SMITS, A. J., SPINA, E. F., ALVING, A. E., SMITH, R. W., FERNANDO, E. M. & DONOVAN, J. F. 1989 A comparison of the turbulence structure of subsonic and supersonic boundary layers. *Phys. Fluids* A **1** (11), 1865–1875.

SORIA, J., SONDERGAARD, R., CANTWELL, B. J., CHONG, M. S. & PERRY, A. E. 1994 A study of the fine-scale motions of incompressible time-developing mixing layers. *Phys. Fluids* **6** (2), 871–884.

SUMAN, S. & GIRIMAJI, S. S. 2009 Homogenized Euler equation: a model for compressible velocity gradient dynamics. *J. Fluid Mech.* **620**, 177–194.

SUMAN, S. & GIRIMAJI, S. S. 2010 Velocity gradient invariants and local flow field topology in compressible turbulence. *J. Turbul.* **11** (2), 1–24.

SUMAN, S. & GIRIMAJI, S. S. 2012 Velocity-gradient dynamics in compressible turbulence: influence of Mach number and dilatation rate. *J. Turbul.* **13** (8), 1–23.

TAYLOR, G. I. 1938 Production and dissipation of vorticity in a turbulent fluid. *Proc. R. Soc. Lond.* A **164**, 15–23.

TSINOBER, A. 2000 Vortex stretching versus production of strain/dissipation. In *Turbulence Structure and Vortex Dynamics*, pp. 164–191. Cambridge University Press.

TSINOBER, A. 2009 *An Informal Conceptual Introduction to Turbulence*. Springer.

VAN DER BOS, F., TAO, B., MENEVEAU, C. & KATZ, J. 2002 Effects of small-scale turbulent motions on the filtered velocity gradient tensor as deduced from holographic particle image velocimetry measurements. *Phys. Fluids* **14** (7), 2456–2474.

VIEILLEFOSSE, P. 1982 Local interaction between vorticity and shear in a perfect incompressible fluid. *J. Phys. Paris* **43**, 837–842.

WANG, B.-C., BERGSTROM, D. J., YIN, J. & YEE, E. 2006 Turbulence topologies predicted using large eddy simulations. *J. Turbul.* **7** (34), 1–28.

WANG, J., SHI, Y., WANG, L.-P., XIAO, Z., HE, X. T. & CHEN, S. 2012 Effect of compressibility on the small-scale structures in isotropic turbulence. *J. Fluid Mech.* **713**, 588–631.

WANG, L. & LU, X.-Y. 2012 Flow topology in compressible turbulent boundary layer. *J. Fluid Mech.* **703**, 255–278.

WU, X. & MOIN, P. 2010 Transitional and turbulent boundary layer with heat transfer. *Phys. Fluids* **22**, 085105.